Ultrasonic Wave-Speed Diffraction Tomography With Undersampled Data Using Virtual Transducers

Fan Shi and Peter Huthwaite

***Abstract*— Ultrasonic diffraction tomography offers a way to achieve high-resolution imaging of the wave-speed map, and hence, has strong potential applications in medical diagnosis and nondestructive evaluation. Ideal images can be obtained with a complete array of sensors surrounding the scatterer, provided that the measurement data are fully sampled in space, obeying the Nyquist criterion. Spatial undersampling causes the image to be distorted and introduce unwanted circular artifacts. In this paper, we propose an iteration approach using virtual transducers to achieve high-resolution tomographic imaging with undersampled measurements. At each iteration stage, the extent constraint estimated from the shape of the object of interest is applied on the image space to obtain a regularized image, based on which the ultrasonic measurement data at virtual transducers are calculated using a forward model. The full data set composed of original and virtual measurements is then used for tomography in the next stage. A final image with sufficiently high resolution is obtained only after a few iterations. The new imaging method yields improvements in the robustness and accuracy of ultrasonic tomography with undersampled data. We present numerical results using complicated wave-speed maps from realistic corrosion profiles. In addition, an experiment using guided ultrasonic waves is performed to further evaluate the imaging method.**

***Index Terms*— Corrosion, tomography, ultrasonic imaing.**

I. Introduction

THERE is considerable interest in quantitative acoustic wave imaging to reconstruct spatial maps of density, stiffness, and sound speed [1]–[3] of an object. One of the most powerful techniques is diffraction tomography (DT). It considers the wave diffraction effects in the algorithm, and hence, generates images with a much higher resolution compared with computed tomography based on the ray tracing assumption [4], [5]. DT has been widely applied in medical ultrasound, as the wave-speed map assists the early diagnosis of, for example, breast cancer [2]. Different ultrasound imaging methods for breast cancer detection have been compared, and the importance of diffraction has been stressed [6]. A multiscale approach for imaging complex 3-D objects using DT has been developed in [7]. A short-scan filtered backpropagation reconstruction algorithm has been employed in [8] for a limited-view imaging problem in DT. In recent years, guided wave DT has been developed for measuring the thickness loss of the pipe caused by corrosion [9], [10]. By fixing the frequency, based on the guided wave dispersion curves, the wave velocity becomes a function of the pipe thickness. Hence, by imaging the distribution of the wave speed using tomography, one can obtain the map of the thickness loss accordingly. Other applications include seismic wave tomography for imaging the subsurface of earth [11] and underwater acoustic tomography for exploration of ocean environments [12]. In this paper, we focus on the application of guided wave tomography to characterize the corrosion profiles.

Under ideal conditions, a complete array surrounding the object with a sufficient number of sensors would be available, and the spatial sampling interval between two adjacent sensors should obey the Nyquist criterion. However, in many scenarios, due to the restrictions such as cost, geometry, and computational power of hardware, attempts have been proposed to reduce the number of sensors by increasing the sampling interval while still maintaining high qualities of images; this is a key technical issue in many fields such as nondestructive evaluation (NDE) [13], [14], medical imaging [15], and seismic wave imaging [16]. Subsampling leads to an underdetermined inverse problem where multiple solutions exist for the same set of measurements. One solution is the "artifact-free" real solution, which we aim for but is challenging to find. Normally, unknown measurement data at missing positions are simply filled with zeros, and this leads to the aliasing effects which greatly pollute the image by introducing coherent artifacts. In order to break the coherence, a random sparse array can be applied for imaging defects in plates with an optimized array layout [14]. Alternatively, researchers have applied the conformal map theory for design of ultrasonic array [17]. Other methodologies include the use of so-called Excitelet to correlate the measurement signals with simulated signals, so that various parameters can be included [13], [18]. It has been shown that fewer sensors are required for imaging, which is mainly caused by the fact that by correlating signals, multiple frequency components are taken into account, and hence, the coherent artifacts are somewhat averaged out. However, these methods are all for structural imaging, from which only the size or the shape of the object instead of quantitative physical properties are reconstructed.

To solve the underdetermined problem for quantitative imaging where the data are undersampled, a powerful

Manuscript received January 8, 2018; accepted April 3, 2018. Date of publication April 19, 2018; date of current version June 26, 2018. This work was supported by the Engineering and Physical Sciences Research Council under Contract EP/M020207/1. *(Corresponding author: Fan Shi.)*

The authors are with the Department of Mechanical Engineering, Imperial College London, London, U.K. (e-mail: f.shi12@imperial.ac.uk).

Digital Object Identifier 10.1109/TUFFC.2018.2828644

approach is to impose some prior knowledge according to the nature of the image. Conventionally, additional information such as positivity, range of magnitude, maximizing entropy, and extent of objects [19] can be incorporated to assist solving the linear matrix system. Normally, the imaging algorithm is implemented as an optimization to seek the best solution to fit the measurement data, combined with a weighted regularization term corresponding to the prior knowledge. In particular, the undersampling issue leads to the vast development of compressive sensing (CS) methods [20]. The CS relies on the L_1 norm minimization [20], [21] instead of the conventional L_2 norm, or the least square technique. It requires for one to identify a sparse representation of the image, and transform the imaging into an optimization problem to find the best matching solution for the sparsity [22]. For instance, CS has been applied in divergent beam current transformer [23], [24] and photography [20] where the L_1 norm or the total variation of image pixels is adopted as the sparse representation. By transforming the image to the wavelet domain, CS can be implemented as minimizing the L_1 norm of the wavelet coefficients as applied in magnetic resonance imaging [25], [26], ultrasonic imaging [3], [27], [28], and photoacoustic tomography [29]. CS is particularly attractive in applications that exhibit high-resolution contrast image features. For more general cases where the variation of image pixels is relatively smooth, CS may not be very effective compared with the conventional imaging algorithms based on the least square concept. In addition, to numerically solve the general optimization problem, one may need to control the variables such as the step size and the weighting of the regularization term, whose best values are often case dependent.

An alternative way to solve the underdetermined problem is the projection method, which avoids the need to solve the whole system as an optimization problem. A typical example is the K-space projection method for DT [15], which iterates between the image space and the K-space using the fast Fourier transform (FFT). At each iteration, the image is regularized according to the prior knowledge, and a new K-space containing compensation for the missing data is formed. The whole process is iterated until the convergence criterion is satisfied. The regularization can be realized by applying the constraint of positivity or extent support of the object [15], [19], [30]. An adaptive thresholding approach has been developed in [31] as a new regularization method to gradually reconstruct the features from low to high contrast. However, all of the above-mentioned methods are implemented for limited-view problems where the data within a range of angles are missing. The projection methods have not been applied to address the undersampled cases with a full-view measurement setup, which is equally important to the limited viewing problems.

In this paper, the projection method is applied for the wave-speed tomography with undersampled data. We do not utilize the widely used K-space projection method, because it is not well suited for near-field data which are often seen in NDE, and the interpolation of the K-space data into a regular grid may also lead to additional errors. Instead, we adopt the idea of virtual transducers. Specifically, the extent constraint is applied to regularize the image, and the measurement data at virtual transducers are calculated using a full numerical model. The complete set of data from both virtual and original transducers is then used for tomography. The iteration is repeated until convergence. In this way, we show that the image quality, especially the resolution, can be significantly enhanced when the measurement data are subsampled. The main motivation of developing the new method is for guided wave tomography of corrosion profiles on pipes, although it is possible to extend and adjust the method to other fields, such as medical ultrasound.

This paper is organized as follows. Section II introduces the background of the DT. Section III illustrates the proposed imaging approach with undersampled data. Numerical examples are presented in Section IV, and experimental results are demonstrated in Section V. Concluding remarks are made in Section VI.

II. Diffraction Tomography

A. Formulation of DT

The measurement setup is depicted in Fig. 1, in which a circular array of sensors is deployed surrounding an inhomogeneous object within a homogeneous background of a constant wave speed c_0. The locations of the transmitters and receivers are denoted as $\boldsymbol{s}$ and $\boldsymbol{r}$, respectively, and the coordinate of a point in the defect is $\boldsymbol{r}_0$. In this paper, we only consider an acoustic medium which simplifies the problem by only supporting compressional waves. Similar imaging procedures can be extended to elastic wave problems in solids [32]. The fundamental acoustic wave equation in the frequency domain with the objective function $O(\boldsymbol{r}_0)$ as a source perturbation is expressed as [33]

$$(\Delta^2 + k_0^2)\psi = -O\psi \tag{1}$$

where the objective function is defined as

$$O(\boldsymbol{r}_0) = k_0^2\Big[\Big(\frac{c_0}{c(\boldsymbol{r}_0)}\Big)^2 - 1\Big]. \tag{2}$$

In (1) and (2), ψ is the acoustic potential of the field, and $k_0 = 2\pi f/c_0$ is the wavenumber of the background where f is the frequency. In guided wave tomography, the attenuation of waves is very low, and hence, is normally not considered to simplify the inverse model [34]. In addition, any density variation is generally neglected; while this can be corrected for [35], this is considered beyond the scope of this paper. The general acoustic wave equation without any source term is

$$\big(\Delta^2 + k_0^2\big)\psi_0 = 0 \tag{3}$$

where ψ_0 represents the background wavefield where no scatterer is presented. The free-space Green's function of the background media, taken as the solution to

$$\big(\Delta^2 + k_0^2\big)G_0(\boldsymbol{r}, \boldsymbol{r}_0) = \delta(\boldsymbol{r} - \boldsymbol{r}_0) \tag{4}$$

is obtained in 2-D as

$$G_0(\boldsymbol{r}, \boldsymbol{r}_0) = -\frac{i}{4}H_0^{(1)}(k_0|\boldsymbol{r} - \boldsymbol{r}_0|) \tag{5}$$

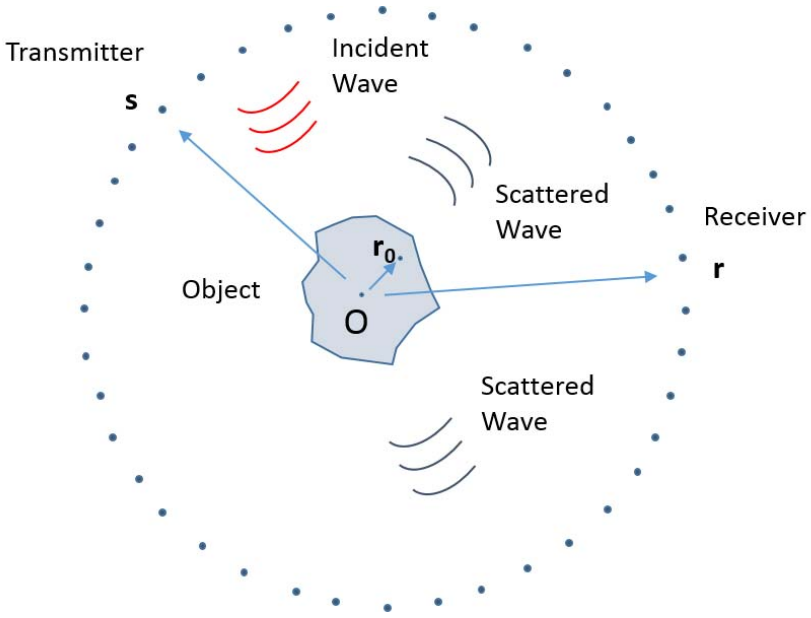

Fig. 1. Measurement setup for ultrasonic DT with a circular array.

where $H_0^{(1)}$ is the Hankel function of the first kind. From (1), (4), and (5), the total wavefield is calculated as

$$\psi = \psi_0 - \int_{r_0} O\psi G_0 d\boldsymbol{r_0} \tag{6}$$

which is called the Lippmann–Schwinger equation.

To invert the objective function, the Born approximation that $\psi \approx \psi_0$, can be applied on the right-hand side of (6), and the following expression is obtained:

$$\psi_s \approx -\int_{r_0} O\psi_0 G_0 d\boldsymbol{r_0} \tag{7}$$

where ψ_s refers to the scattered field which equals $\psi - \psi_0$. By assuming a point sourcelike transmitter, ψ_0 in (7) can be replaced with the Green's function G_0, which leads to

$$\psi_s(\boldsymbol{r}, \boldsymbol{s}) \approx -\int_{r_0} G_0(\boldsymbol{r}, \boldsymbol{r}_0) O(\boldsymbol{r}_0) G_0(\boldsymbol{s}, \boldsymbol{r}_0) d\boldsymbol{r_0}. \tag{8}$$

By integrating ψ_s in (8) along the apertures for all possible transmitters and receivers, an image can be obtained with the conventional beamforming (BF) algorithm

$$I^{\mathrm{BF}}(z) = \int_s \int_r \frac{\psi_s(\boldsymbol{r}, \boldsymbol{s})}{G_0(\boldsymbol{r}, \boldsymbol{r}_0) G_0(\boldsymbol{s}, \boldsymbol{r}_0)} d\boldsymbol{r} d\boldsymbol{s}. \tag{9}$$

The above-mentioned integral is numerically calculated as a discrete sum. The objective function from BF is a distorted version of the DT reconstruction as stated in [36]. To obtain the correct image, one can apply a filter to the Fourier transform of the BF image taking the weighted coefficient into account, and then transform the spectrum back to the spatial domain to generate the DT image. The details of this filtering approach are illustrated in [36], and it is also valid when the measurement is performed in the near field [37].

B. HARBUT

The Born approximation (e.g., $\psi \approx \psi_0$) is valid when the phase error is small for the wave traveling through the object, and hence, is not suitable for more general situations where the wave-speed contrast is high. Advanced tomography algorithms such as the distorted Born iterative method [38] and the more recently developed hybrid algorithm for robust breast ultrasound tomography (HARBUT) [2] are effective to address high-contrast imaging problems. It first estimates an inhomogeneous background and then performs the imaging of the small perturbation from the background with the conventional DT algorithm. In this manner, HARBUT can accurately reconstruct the objective function beyond the valid region of the Born approximation.

According to [2], the BF image of the perturbation from the inhomogeneous background is

$$I_\delta^{\mathrm{BF}}(z) = \int_s \int_r \frac{\psi_\delta(\boldsymbol{r}, \boldsymbol{s})}{G_b(\boldsymbol{r}, \boldsymbol{r}_0) G_b(\boldsymbol{s}, \boldsymbol{r}_0)} d\boldsymbol{r} d\boldsymbol{s} \tag{10}$$

where G_b is Green's function in the inhomogeneous background, which is different from G_0 in (4). $\psi_\delta = \psi - \psi_b$ is the perturbation of the wavefield relative to the background. In fact, we can substitute ψ instead of ψ_δ into (10), as shown in [2] and [37], and it is numerically more convenient as calculating ψ_δ is not straightforward. The filtering approach, as used in [36], for the conventional DT algorithm can be equally applied on (10) to obtain the corrected image. The HARBUT image is then the superposition of the background and the reconstructed correction image from DT. Note that the image quality of the background is not critical for the whole method, and hence, the bent ray tomography (BRT) algorithm [39] is used as it gives a reasonable low-resolution background image. In addition, the obtained image can be used as a new inhomogeneous background for the next stage of HARBUT so that the algorithm can be used with several iterations to obtain the final image.

C. Undersampling Effect

To avoid the aliasing effects, it is well known that for a linear array, the spatial sampling interval needs to be less

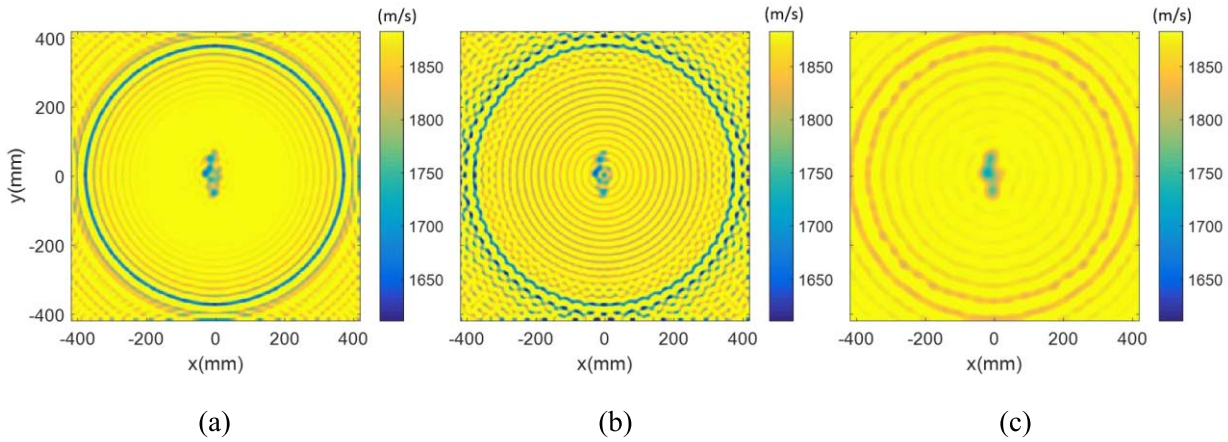

Fig. 2. Effects of subsampling for DT images. (a) DT image from fully sampled data. (b) DT image from subsampled data. (c) DT image from subsampled data after applying a low-pass filter.

than half wavelength $\lambda/2$ [40]. Similar criterion is obtained by Huthwaite [37], which shows that the separation distance of sensors for a circular array, as depicted in Fig. 1, needs to satisfy the following expression:

$$\frac{|\boldsymbol{K}|}{2k_0} = \frac{\lambda/2}{\Delta_{\text{lim}}}. \tag{11}$$

The above-mentioned sampling criterion is derived from the spatial sampling of the total field for imaging (i.e., scattered field + incident field). A more relaxed sampling criterion using the purely scattered field for the circular array is explained in [40]. However, in this paper we decide to use (11) considering the effects from the incident wave because in a real measurement, it is hard to separate the incident wave field from the total field for imaging, especially when the transducers are placed in the near field.

In (11), $\boldsymbol{K}$ denotes the spatial frequency and Δ_{lim} is the required spatial gap between two neighboring transducers to avoid any aliasing effects. The maximum spatial frequency of an image obtained from any linear algorithm is $2k_0$ based on the Ewald disk [31], which results in $\Delta_{\text{lim}} = \lambda/2$ as expected. Equation (11) can also be written in another way for a fixed value of the spatial interval Δ as

$$|\boldsymbol{K}_{\text{lim}}| = \frac{\lambda k_0}{\Delta}. \tag{12}$$

Equation (12) indicates that the spatial spectrum of the image should be correct when $\boldsymbol{K}$ is smaller than $\boldsymbol{K}_{\text{lim}}$, By applying a low-pass filter to the image, artifacts caused by aliasing can be eliminated with a penalty of reducing the resolution.

Examples are presented in Fig. 2 to illustrate the spatial undersampling effect. The object to be reconstructed is a wave-speed map converted from the thickness profile of a typical corrosion sample from industry. A circular array of transducers with an equal distance of 380 mm away from the object is deployed. All the transducers send and receive ultrasonic waves which are then used for tomography. The background wave speed is 1883 m/s and the frequency is assumed to be 50 kHz. Fig. 2(a) shows the reconstruction results with a fully populated array of 128 transducers, while the undersampled case with 64 transducers is shown in Fig. 2(b). Clearly, undersampling leads to circular artifacts caused by aliasing, which significantly distorts the object of interest. However, these artifacts can be greatly reduced in Fig. 2(c) by applying a low-pass filter with a cutoff frequency $|\boldsymbol{K}_{\text{lim}}| = k_0$ calculated from (12). It is noted that the artifacts always have smaller wave-speed contrast than the object of interest.

III. DT With Virtual Transducers

A. Overall Methodology

In this section, we introduce an iterative method including regularization to address the undersampling problem. The missing data are effectively "interpolated" by placing virtual transducers between adjacent sensors. The whole iteration scheme is described as a flowchart in Fig. 3(a). In the first step, the undersampled data are used to obtain a raw image with a low resolution by applying a low-pass filter according to (12). In the second step, this low-resolution image is set as the initial image O_{in}, and a chosen regularization method is applied to obtain a regularized image, which is denoted as O_{reg}. In the third step, a forward modeling tool, either analytical or numerical, is then implemented based on the object from the regularized image to calculate the measurement data at virtual transducers. These virtual transducers are typically placed in between the original transducers as shown in Fig. 3(b). Therefore, a mixed data set composed of original and virtual measurement data is obtained, which is used for imaging again. This process is repeated with several iterations until convergence. This iterative scheme is general, hence, there is no strict rule for choosing a particular forward model or inverse imaging algorithm. We apply the iterative scheme focusing on the guided wave tomography, for scatterers with general features of corrosion patches, such as the example shown in Fig. 2. Typical corrosion profiles encountered in nondestructive testing usually have smoothly varying surfaces and are embedded in a homogeneous background with a constant wave speed. Hence, they may differ from more complex objects in human bodies, and we do not intend to cover the cases in medical ultrasonic tomography. The overall method is proposed and tested based on realistic corrosion patches from petrochemical industries.

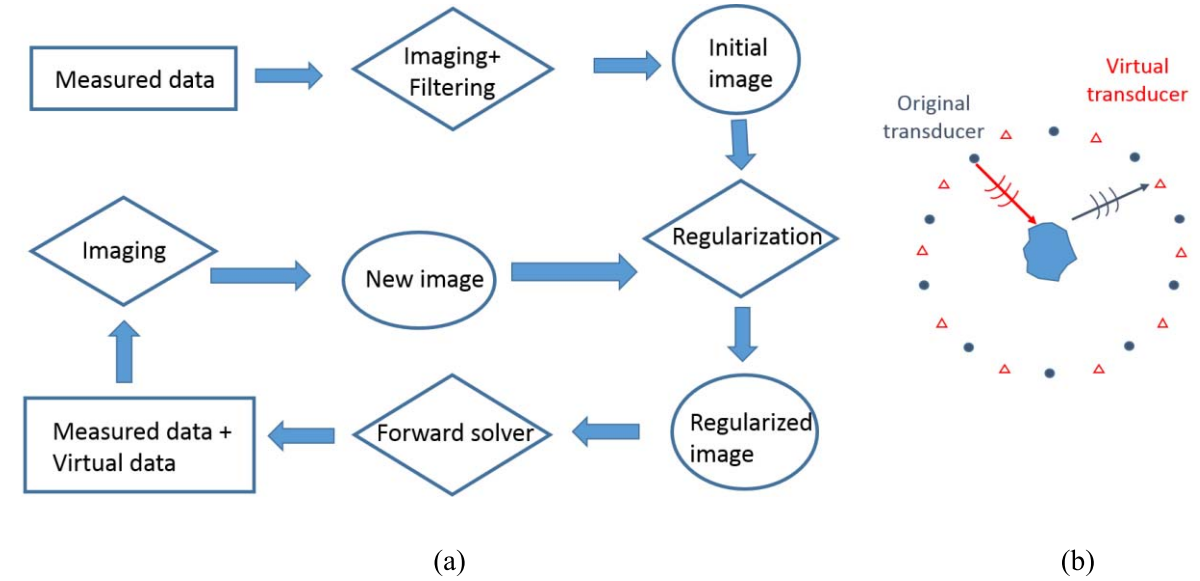

Fig. 3. (a) Flowchart explaining the proposed imaging method in this paper. (b) Illustration of DT using predicted measurements at virtual transducers.

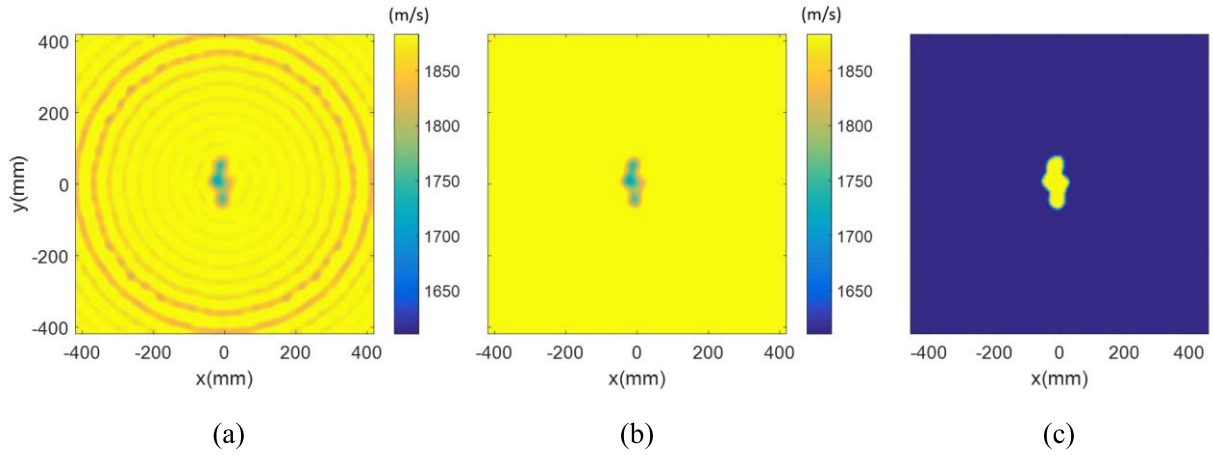

Fig. 4. Illustration of the regularization. (a) Raw initial image from subsampled data after applying a low-pass filter. (b) Regularized image from (a) by using an amplitude threshold. (c) Extracted shape of the object of interest from (b).

B. Regularization

Regularization is a key step during the iterative scheme, as it affects the convergence toward an accurate solution. There are many types of regularization methods based on prior knowledge, such as positivity, amplitude range, adaptive amplitude threshold, and extent constraint. Fig. 4(a) shows a typical raw image from DT using undersampled measurement data. As can be seen, by applying the low-pass filter, the object of interest can be clearly seen although the circular artifacts do not completely disappear. However, the contrast of these artifacts is much smaller compared with the object of interest in the image. Based on this observation, we decide to apply the extent constraint, given that the rough shape of the object can be approximately extracted from the image, by simply applying an amplitude threshold. The actual value of the threshold needs to be set case by case, but it can be easily determined by observing the raw image such as Fig. 4(a). The actual threshold used in the simulations is 98% of the background wave speed. Values larger than the threshold in the image (which are likely to correspond to the artifacts) will be set to the background wave speed c_0. The four corrosion surfaces tested here are shown in Fig. 5, and are generated from laser scanning of true corrosion maps from real pipes used in industry. From the velocity values shown here, the amplitude threshold is applicable to extract the rough extent of the object, for our main application of guided wave tomography of corrosion patches. The image after applying the threshold is shown in Fig. 4(b), which serves as the initial image to run the forward simulation. The extracted extent of the object from Fig. 4(b) is presented in Fig. 4(c), and the values of pixels are unity inside the object and zero otherwise. This image is then blurred by using a Gaussian filter of radius λ to smooth the edge at the object boundary. The regularization at each iteration is realized by multiplying the tomographic image with the blurred image of the object extent.

C. Convergence

The convergence of the iteration scheme is considered as a reduction of the L_2 norm or the energy of the error, similar with the quantity used for limited-angle problems [41].

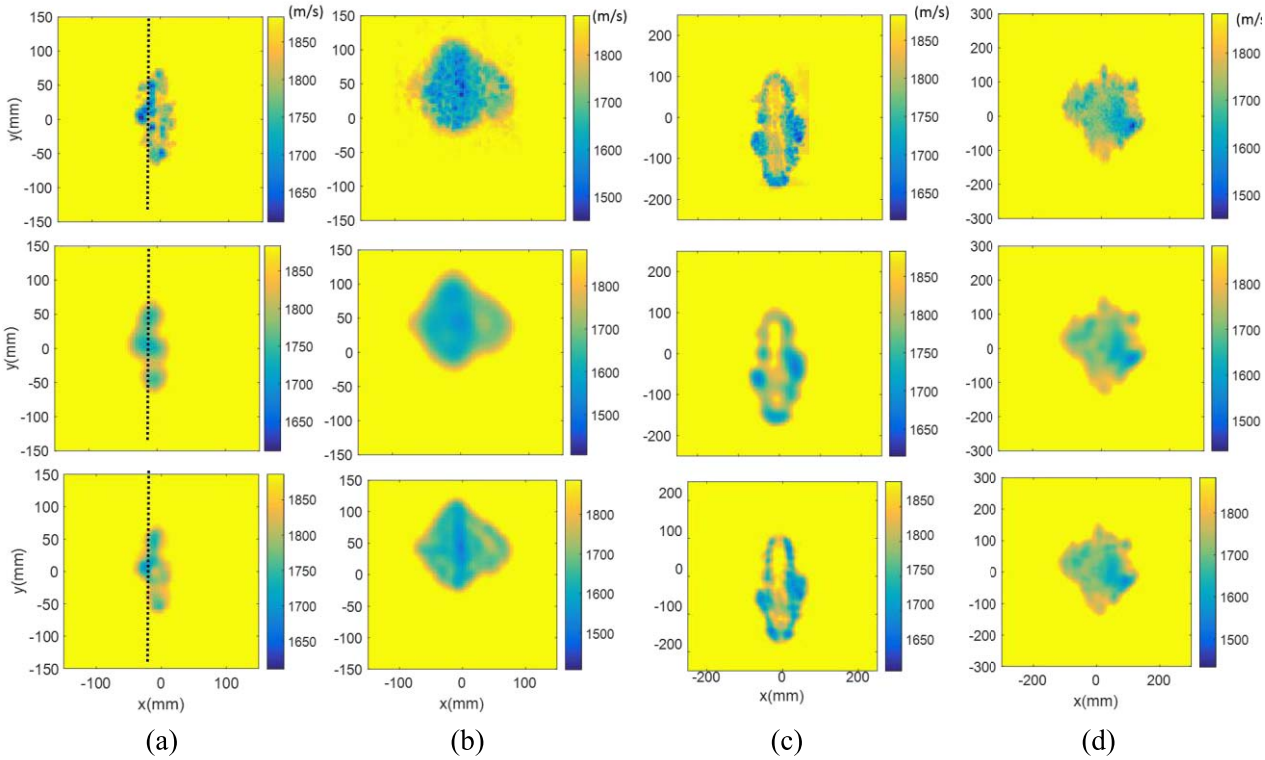

Fig. 5. Imaging results (first row: original wave-speed map; second row: initial images; third row: final images using the virtual transducer technique after five iterations). (a) Wave-speed map 1. (b) Wave-speed map 2. (c) Wave-speed map 3. (d) Wave-speed map 4. For all cases, a clear improvement of resolution can be seen for the third row of images.

To illustrate the convergence, we decided to use the Fourier diffraction theory by linearizing the problem with the Born approximation. It can be argued that the Fourier diffraction theory is not valid for high-contrast problems which are always nonlinear. However, it can give the reader a qualitative explanation why, by compensating missing data from virtual transducers, the final image will be improved.

Here, we define R as the regularization operator, and hence, $RO_{n-1}(x, y)$ means the regularized image of $O_{n-1}(x, y)$ at the $(n-1)$th iteration step. In addition, we define the scattering field $\psi(k_x, k_y)_{n-1}$ as the Fourier transform of $RO_{n-1}(x, y)$. The Parseval theorem [42] guarantees that the L_2 norm in the Fourier domain is equivalent to that in the image domain. The energy of error between the original and reconstructed objective functions can be expressed as

$$\begin{aligned}
&\int\int |O^{\text{original}}(x, y) - O_{n-1}(x, y)|^2 dxdy \\
&> \int\int |O^{\text{original}}(x, y) - RO_{n-1}(x, y)|^2 dxdy \\
&= \int\int |\psi^{\text{original}}(k_x, k_y) - \psi_{n-1}(k_x, k_y)|^2 dk_x dk_y \\
&> \int\int |\psi^{\text{original}}(k_x, k_y) - (\psi_{n-1}^{\text{virtual}}, \psi^{\text{original}})|^2 dk_x dk_y \\
&= \int\int |O^{\text{original}}(x, y) - O_n(x, y)|^2 dxdy. \qquad (13)
\end{aligned}$$

In (13), $(\psi_{n-1}^{\text{virtual}}, \psi^{\text{original}})$ refers to a mixed measurement data set including both virtual and original data. The intial model at the first iteration $O_0(x, y)$ is obtained by applying a low-pass filter to the raw image as shown in Fig. 2(b) and (c). The intial model has a low resolution while maintaining the main features, and hence, is good enough to achieve convergence after a few iterations. Note that when deriving (13), we have used the fact that the regularization $RO_{n-1}(x, y)$ will reduce the error. By observing Fig. 4(a) and (b), it can be noticed that the artifacts are located outside and do not affect the object. These artifacts increase the L_2 norm error between the original and the reconstructed images. By eliminating the artifacts in Fig. 4(a) with the regularization operator, the error will be reduced. In addition, it is a crucial step to mix the original measurement data with the virtual data to form a new data set $(\psi_{n-1}^{\text{virtual}}, \psi^{\text{original}})$, which further reduces the error. If the projected measurement data from the regularized image (ψ_{n-1}) at the original transducers are not replaced by the realistic data, the reconstructed image at the next iteration will not change. Equation (13) shows that the energy of the error is reduced at each iteration step, and hence, the convergence of the scheme is briefly explained here. In Section IV, we will also show the convergence including the effect from the noise using numerical examples. Numerical simulations will be run including all the wave physics, and the trend of convergence will be shown to still hold. Note that the actual fraction of undersampled data will affect the convergence and the ultimate quality of the image. For the case when very less measured data are available, the iteration scheme may lead to reconstructed images with poor resolution.

In the following simulations, we only test the case when the data are downsampled by half to show the efficiency of the proposed imaging method.

IV. Numerical Results

In this section, numerical simulations are performed with four wave-speed maps, as shown in the first row in Fig. 5, to evaluate the proposed imaging scheme. Note that in this paper, we are mainly concerned with the application of guided wave tomography of corrosion profiles. Hence, these wave-speed profiles are generated from the thickness loss map due to corrosion on the pipe [9] using the fundamental A_0 mode dispersion curve. The details of convertion between the wave-speed map and the thickness loss are described later. The four corrosion profiles are measured from the real corrosion from the petrochemical industry, with extents of around 60–200 mm. Much smaller corrosion defects such as pitting defects are not considered in this paper. We utilize these profiles to simulate the measurement data and generate tomography images. At this point, acoustic assumptions are made for both forward simulations and inverse reconstructions. The finite difference (FD) scheme is used for simulating the full wave scattering, and the inverse imaging is performed with HARBUT algorithm, which is valid for imaging realistic objects with high contrasts. A Q factor [34] is used to establish a criterion for the convergence of the iteration scheme

$$Q_n = \frac{\int |c_n(x,y) - c_{(n-1)}(x,y)| S(x,y) dxdy}{c_0 \int S(x,y) dxdy} \tag{14}$$

where $c_n(x,y)$ and $c_{(n-1)}(x,y)$ are the recovered wave-speed maps at the nth and the $(n-1)$th iterations, respectively, and $S(x,y)$ describes the potential location and area of the scatterer, which is defined as

$$S(x,y) = \begin{cases} 1, & \dfrac{c_0 - c_n(x,y)}{c_0} \geq 0.03 \\ 0, & \dfrac{c_0 - c_n(x,y)}{c_0} < 0.03 \end{cases} \tag{15}$$

The Q factor represents the relative change of the wave speed between iterations over the area of the scatterer, normalized by the background wave speed c_0. In the following numerical simulations, we run iterations until the Q factor is less than 5×10^{-4}, indicating that the convergence is achieved.

The background wave speed is 1883 m/s and the frequency of incident waves is 50 kHz. A circular array composed of 64 transducers is placed 380 mm away from the object; the far-field approximation is not applicable in such a small distance. By using (12), it is found that for the array configuration here, the critical value of $K_{\lim}$ is k_0, above which the aliasing occurs and the high-frequency components of the image are not accurate. A low-pass filter is, therefore, applied to mitigate coherent artifacts, and a low-resolution initial image is obtained as an input to the iteration scheme. A FD code as implemented in [43] is used to fully simulate the acoustic wave scattering, The FD code is based on a staggered grid mesh, and the perfect matched layer (PML) technique [44] is adopted to eliminate the artificial wave reflections from boundaries. The grid spacing is 0.003 m ($\approx 1/12\lambda$), and the thickness of PML is 0.06 m. All the complex acoustic wave scattering is included once the convergence of the FD scheme is achieved. A five-cycle Hann-windowed tone burst with a center frequency of 50 kHz is assumed to be the input signal for each transmitter. The FD code is programed in the frequency domain, hence, to calculate the measurement signals, we run the code 63 times corresponding to frequencies from 20 to 80 kHz with a separation of approximately 970 Hz. A loop of simulations is run using the FD code with different frequencies and the inverse FFT is then used to obtain the time-domain signals scattered from the object.

For the reconstruction, the HARBUT algorithm is used to account for the high velocity contrast between the background and the object. The FD code is also implemented as a forward model at the center frequency to compute the scattering at virtual transducers. Similar to the virtual image space component iterative technique approach applied in [31], now we have two iterations to run: HARBUT with iterations to update the background image, and compensation at virtual transducers from the regularized image using the FD forward model. In this paper, for convenience, we choose to perform HARBUT iterations within one iteration of virtual transducers, because in this manner, we can reduce the number of running forward numerical simulations.

In the full implementation, arrival times extracted from simulated measurement waveforms are used to obtain the background image with the BRT algorithm. Undersampling also contributes to artifacts in the BRT images, and a spatial Gaussian filter of radius λ is applied to blur the BRT background to reduce artifacts. HARBUT algorithms are then applied on the BRT background to obtain the initial low-resolution image as an input to the iteration scheme using virtual transducers. The extent of the object is extracted from the initial image by applying an amplitude threshold, and it is used for regularizing the image at each iteration of virtual transducers. The FD simulation is performed on the regularized image to obtain the measurement field at the virtual transducers at the center frequency 50 kHz. The fully populated measurement data are then used for HARBUT imaging again for the next stage of iteration. The number of iterations to achieve the required image quality depends on the actual wave-speed profile, and normally six to ten iterations are sufficient for all cases tested in this paper.

The final images obtained after six iterations along with the original maps and initial images are shown in Fig. 5. For comparison, we show the low-resolution initial image without any iteration. Clearly, the initial images (second row) of Fig. 5(a)–(d) fail to capture the details of the wave-speed map. The proposed method improves the resolution of the reconstruction for all four cases. The recovered images are artifact free, and reveal much finer details of the object. This is natural because by compensating for the missing measurement data at the virtual transducers, there is no need to apply the low-pass filter with a cutoff frequency of k_0 for the image. The additional high-frequency components between k_0 and $2k_0$ result in improved resolution.

Furthermore, the 1-D cross section profiles of the reconstructed wave-speed maps extracted along the dotted line in Fig. 5(a) are presented in Fig. 6. The proposed method

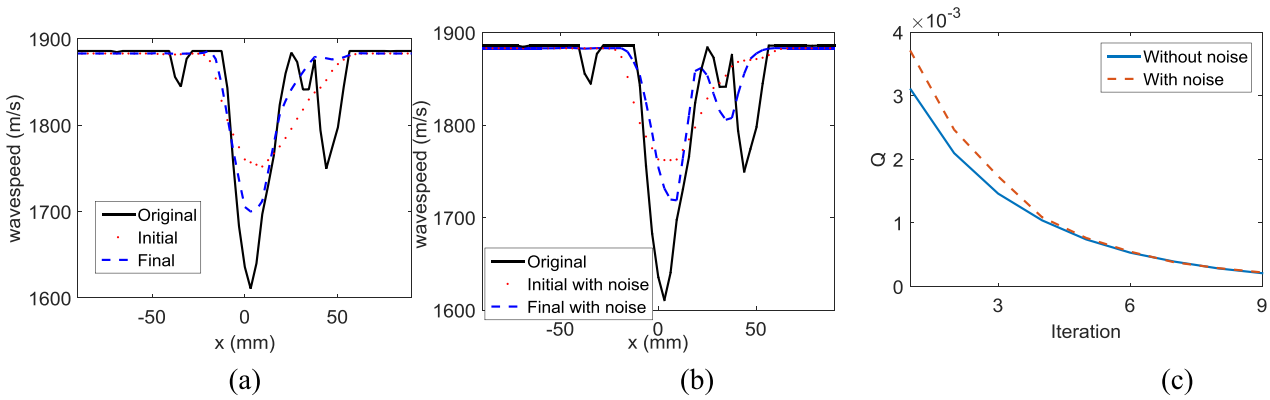

Fig. 6. (a) Plot of the 1-D cross section profiles of the wave-speed map 1 along the black dotted line in Fig. 5. (b) Plot of the same 1-D cross section with artificial noise added to the data. (c) Convergence Q factor of wave-speed map 1 with and without the noise.

contributes to a more refined overall shape of the profile in comparison with that from the initial image, and also a more accurate reconstruction of the extreme value of the wave speed. The minimum value of the wave speed is crucial in many engineering applications such as guided wave inspection of corrosion, because it corresponds to the minimum thickness of the pipe wall, which strongly affects the remaining lifetime of the pipe. Reconstructing the minimum value is associated with the resolution, given that a poor resolution is more likely to miss or severely underestimate the "peak" or "valley" of pixels in the image. Therefore, the proposed iterative scheme results in a higher resolution as well as a more accurate estimation of the extreme value. Note that even a perfect linear DT reconstruction has a resolution limit of spatial frequencies up to $2k_0$ [31], and hence, it is expected that HARBUT may underestimate the minimum wave speed located at very sharp "valleys."

In addition, an artificial noise matrix is added to test both the reconstruction and the convergence. Specifically, the real and imaginary parts of the random noise matrix both have a normally distributed amplitude with rms 5% that of the original measurement matrix. The 1-D reconstructed profile with the random noise is shown in Fig. 6(b). Furthermore, in Fig. 6(c), we present the Q factor defined in (14) as a function of number of iterations, and the results are seen to converge well with and without the random noise. Good trends of convergence can be found for all the four numerical examples tested in this paper. It may be argued that the use of FD code in both the forward and inverse modeling stages may run the risk of the inverse crime and an independent numerical method may be more appropriate. However, it is the HARBUT algorithm which is used for inversion directly rather than the FD formulation. HARBUT is actually a nonlinear adapted method based on the Fourier diffraction theory. Besides, once the convergence is achieved, the simulation results would not change when replacing the FD code with a different numerical scheme such as finite element (FE). The effects of noise on the reconstruction are also presented. Hence, the risk of inverse crime is avoided.

V. Experiment

An experiment is conducted to further evaluate the proposed imaging approach using an inhomogeneous sample with spatially varying wave speed. The sample can be manufactured, for instance, by carefully filling the background agar slab with ethanol–water mixtures [31], which gives a distribution of wave-speed values directly due to the material difference between injected inclusion and the background medium. In this paper, an alternative experimental setup is applied by using the guided wave tomography technique, which is the main motivation to develop the new method for the use in NDE. Specifically, the sample plate is manufactured with a varying thickness profile, corresponding to variations of wave velocities according to the A_0 mode dispersion curve in Fig. 7(a). For a fixed frequency, there is a one-to-one mapping between the phase/group velocity and the thickness for a particular mode. In this manner, a wave-speed map is created and we aim to obtain the image of the wave speed and then the thickness.

A. Full Simulation of Guided Wave Tomography Experiments

First, we perform 3-D FE simulations of the measurements of A_0 mode guided waves scattered from a realistic corrosion patch. The motivation is to simulate, as closely as possible, a real experimental setup of guided wave tomography on a platelike structure, as shown in Fig. 7(b). The material for the plate is assumed to be aluminum (Young's modulus: 70 GPa; density: 2700 kg/m^3; and Poisson ratio: 0.33). The dimension of the FE domain of the plate is 1050 × 1050 × 10 mm^3 (length × width × thickness), and absorbing layers [45] with a length of 120 mm are added surrounding the simulated plate to eliminate any unwanted reflections from the edges. The whole FE domain is meshed with eight-node hexahedron elements, and the corrosion region is meshed by squashing the elements according to the thickness [32]. The mesh profile of the corroded region in the plate is shown in Fig. 8(a). The realistic corrosion profile is chosen to be patch 4 shown in Fig. 5(d). A circular array of node points located 380 mm away from the center of the plate is selected as point sources to transmit A_0 mode guided waves, by forcing the motion in the z-direction perpendicular to the plate. The same set of nodes are used as receivers to record the scattered waves from the corrosion. A five-cycle tone burst with a center frequency of 50 kHz is used as the input signal at each point source.

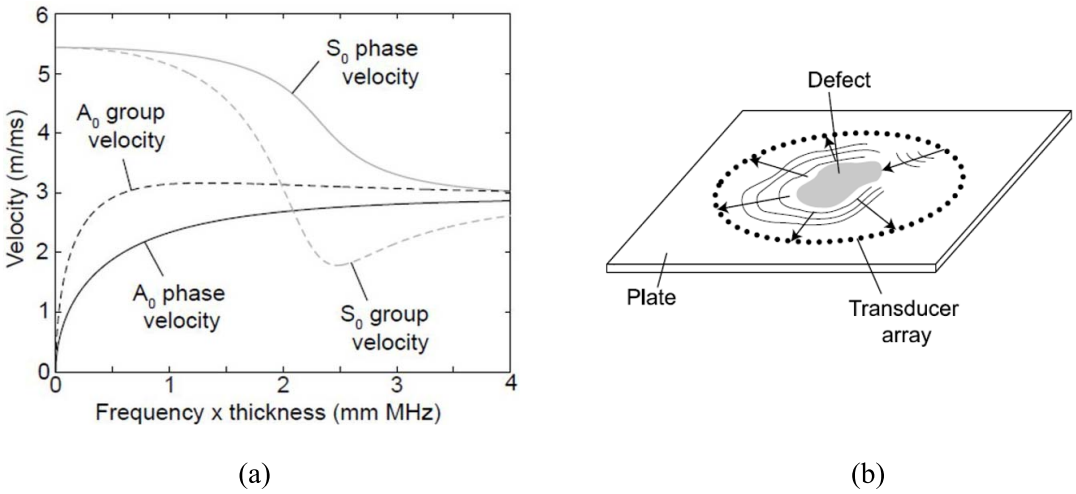

Fig. 7. (a) Dispersion curves of fundamental guided wave modes in an aluminum plate. The phase/group velocity is a function of frequency and thickness. (b) Sketch showing the FE simulation of guided waves sent by multiple transmitters, scattered by the corrosion patch, and measured by multiple receivers.

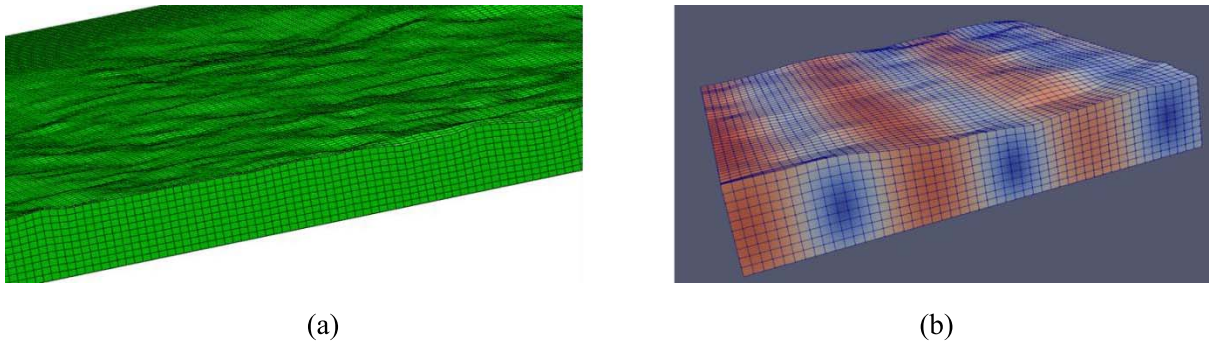

Fig. 8. (a) Local mesh of the plate in the region of the corrosion. Eight-node hexahedral elements are squashed to mesh the irregular corrosion. (b) One snapshot of animation showing the A_0 guided wave propagation through the corroded area in the plate.

The number of transducer/receivers in the simulation is 64, in order to match the experimental setup of measurements in the later section. The measured signals are transferred to the frequency domain, and the components at the center frequency (50 kHz) are extracted to compose a measurement matrix (64 $\times$ 64), including the incident field. An artificial noise matrix with a normal distributed amplitude with rms 5% that of the original measurement matrix is added to evaluate the reconstruction results. The 3-D FE models are run using an accelerated FE software Pogo with GPUs [46], and the simuated wavefield of the propagated guided waves through the corroded plate is shown in Fig. 8(b). The FE model has been widely used for a number of ultrasonic simulations, including ones for guided wave tomography, and has been extensively validated (e.g., [43]). The approach captures the full physics of guided wave scattering and the addition of noise makes the data highly representative of true measurements. The use of a different forward model also helps to avoid any question around the so-called "inverse crime," where the same model is used both in data generation and inversion. Given the high fidelity demonstrated of these modern modeling techniques, this is considered a suitable alternative to a full experimental setup for a complex defect, augmenting the simpler experimental validation with circular defects shown in the later section.

By downsampling the measurement matrix by a factor of two, a new matrix (32 $\times$ 32) is used to evaluate the imaging method. A wave-speed map is first obtained from HARBUT, which is then converted to the thickness map of corrosion according to the A_0 mode dispersion curve. Fig. 9(a) shows the inital thickness map using 32 transducers. A clear improvement in terms of both shape and values of the images can be seen in Fig. 9(b), by using the virtual transducers after six iterations. For comparison, we also plot the reconstructed thickness map using the 64 transducers in Fig. 9(c) (e.g., without downsampling). As can be seen, by using the virtual transducers, the recovered image with 32 transducers matches well with that with 64 transducers. The 1-D cross section profiles of the reconstructed thickness maps when $x = -20$ and 95 mm are plotted in Fig. 9(d) and (e). The proposed new method captures well the variations of the thickness map, and also recovers more accurately the maximum values of the thickness reduction. It is noted that the reconstructions do not capture exactly the deepest point

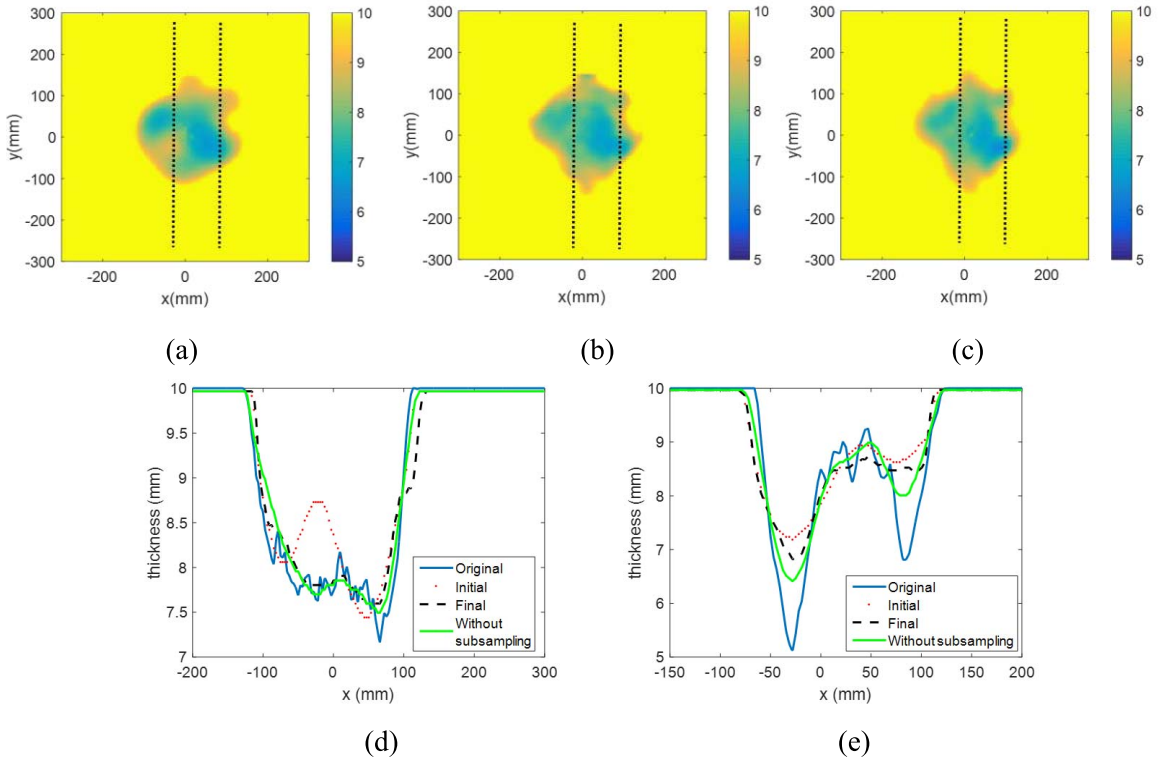

Fig. 9. Imaging results for simulations of guided wave tomography of a realistic corrosion profile. (a) Initial thickness map with 32 transducers. (b) Final thickness map after five iterations using virtual transducers with 32 transducers. (c) Thickness map with 64 transducers (reference case without subsampling). (d) Plots of the 1-D cross section profiles of the thickness map when $x = -20$ mm [left black dotted line in Fig. 11(a)–(c)]. (e) Plots of the 1-D cross section profiles of the thickness map when $x = 92$ mm [right black dotted line in Fig. 11(a)–(c)].

(e.g., the maximum thickness loss). This is because the acoustic assumption results in a limit of the imaging resolution of around two wavelengths [9]. However, the resolution can be improved by correcting the density [35] and using an elastic wave model [32].

B. Experimental Setup

The actual experiment work of guided wave tomography was performed by Belanger *et al.* [47]. The experimental configuration is shown in Fig. 10, with an aluminum plate of $1200 \times 1200 \times 10$ mm^3. The plate is large enough to reduce the effects of reflections from the edges. Two circular defects are created with different depths and diameters: defect A—50% (5 mm) depth and 60 mm diameter; defect B—30% (7 mm remaining) and 100 mm diameter. A single transducer 400 mm away from the center of the plate is used to transmit A_0 mode guided waves, and the total wave field displacement at locations of the receiver array is measured by a Polytec OFV-505 laser Doppler vibrometer [47]. The modeled receiver array is composed of 64 "sensors" and is placed as a semicircle confronting the single transmitter. The transmission waves are effectively recorded while most of the reflections are lost. The source is then taken to the next position with the receiver array moving accordingly. By repeating this procedure, the full matrix capture of measurements with all the send–receive combinations is obtained. A five-cycle

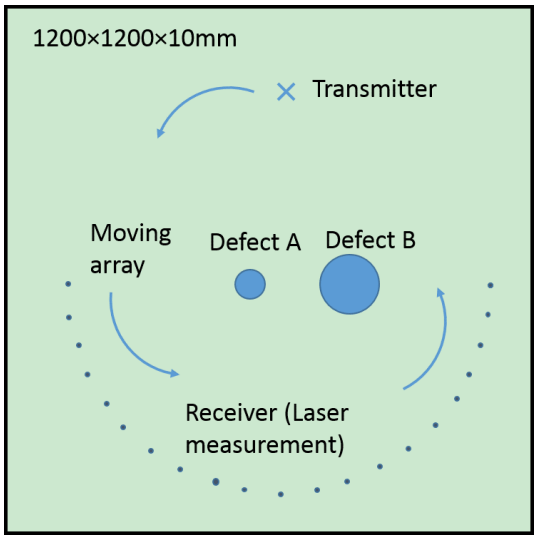

Fig. 10. Illustration of the experimental setup and the sample plate. Defect A located in the center has a diameter of 60 mm and depth of 5 mm. Defect B offset from the center by 200 mm has a diameter of 100 mm and depth of 3 mm (7 mm remaining). Both the transmitter and the semicircle array of receivers are moving to produce the measurement matrix at different angles. The transmitted waves at receivers are measured by a Polytec OFV-505 laser Doppler vibrometer.

Hann-windowed tone burst with a center frequency of 50 kHz is used as the excitation signal. Note that due to the reflective

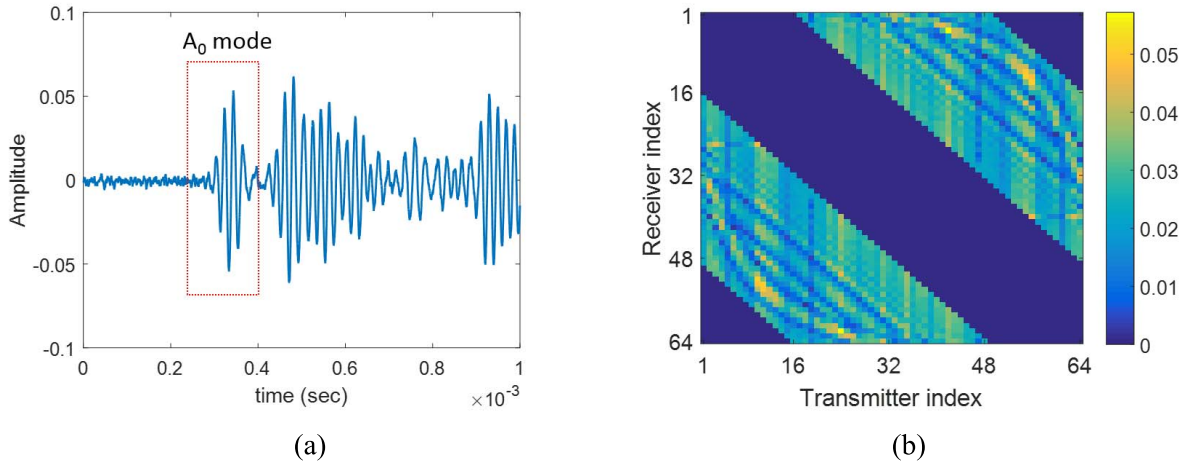

Fig. 11. Processing measured signals. (a) Apply a window to gate the A_0 mode signals in the time domain. (b) Extracted measurement matrix as a function of transmitter and receiver index at the center frequency 50 kHz. The measurement matrix contains both incident and scattered waves.

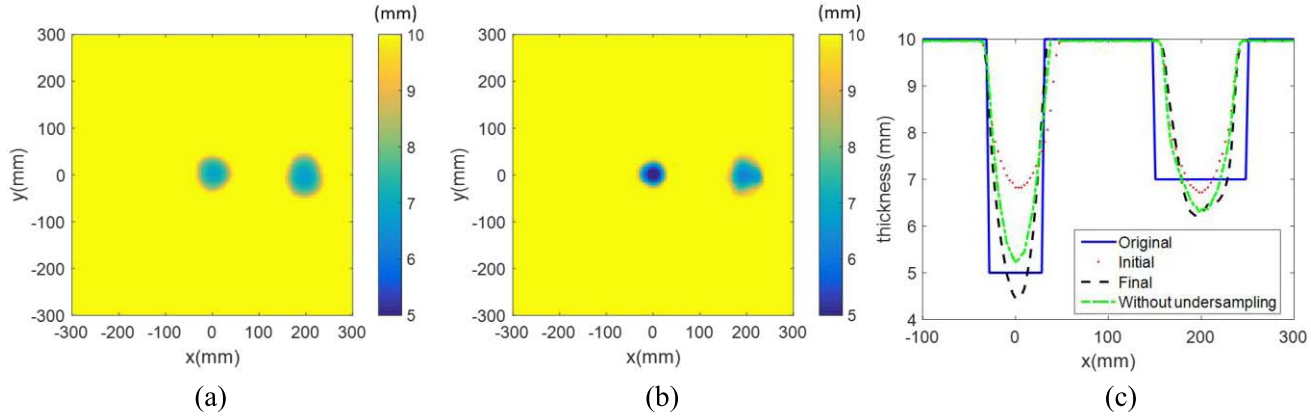

Fig. 12. Experimental results. (a) Initial image from DT. (b) Final image using the virtual transducer technique after seven iterations. (c) 1-D cross section of the reconstruction along the center line of the image.

symmetry of the sample, the source is only scanned around half of the array and this data is then replicated.

C. Signal Processing

A typical received signal is shown in Fig. 11(a), containing multiple guided wave modes, and also the reflections of incident signals from sensors and plate boundaries. We first use a time window to gate the pure A_0 mode signal from the estimation of its time of arrival from the group velocity. Envelopes of signals are obtained by using the Hilbert transform, and the arrival times are taken at the threshold of 30% of the wavepacket's peak amplitude. The values of arrival times are passed to the BRT algorithm to reconstruct a low-resolution background image. Note that the image formed directly from BRT is the group velocity map, being based on the arrival times of the wave packets, which needs to be converted to a phase velocity map for the use of HARBUT.

The time-domain signals are then transformed into the frequency domain, from which the component at the center frequency f_{cen} is extracted, and can be stored in the form of the measurement matrix corresponding to all transmitter–receiver pairs. The calibration procedure is similar with that shown in [31]. Specifically, by observing the matrix, we can identify components that correspond to waves directly received by the receiver without any interaction with the object. These components always appear where straight ray paths of send–receiver pairs do not intersect the confined object, and they can be used as the pure incident wave field when the scatterer is not present. The incident field can be normalized by the Green's function in (5) to approximately estimate the amplitude of the input signal of the transmitter. The measurement matrix is then normalized by the input amplitude to obtain the actual frequency response as shown in Fig. 11(b). Each element in the full data matrix refers to one pair of transmitter and receiver. In the experiment, only the transmission waves, when the transmitter and the receiver are placed, on two sides of the object are recorded. The reflection is not measured, hence, contributing to zero components in the matrix as shown in Fig. 11(b). The measurement matrix is then downsampled by a factor of two (64–32 transducers) to test the proposed imaging approach.

D. Results

The subsampled measurement matrix (32×32) is used to generate a raw initial image, as an input for iterations using virtual transducers. The final image is then converted to a thickness map according to the dispersion curve. Fig. 12 shows the low-resolution initial image and the final image after five iterations. A prominent enhancement of the reconstruction can be observed using the proposed imaging method by comparison with the initial image. The 1-D cross section lines at the center of images are plotted in Fig. 12(c), and for comparison, we show the reconstructed result using the data from 64 sensors without subsampling. It can be found that the initial image only gives the rough shape of the two defects, while severely underestimating the values of the thickness loss, especially for Defect A with an error of 2 mm. In contrast, the proposed method accurately estimates the minimum thickness by significantly reducing the error to around 0.5 mm.

VI. Conclusion

In this paper, we develop an imaging method using virtual transducers to address the undersampling problem for ultrasonic DT. The raw image formed directly from the undersampled data after applying a low-pass filter is used as the input of the imaging scheme. The extent of the object is extracted, and it is used as a spatial filter to regularize the image at each iteration stage. A forward numerical model is run on the regularized image to calculate the measurement signals at virtual transducers, to form a complete set of data in conjunction with original measurements for tomography. In this manner, the true objective function can be iteratively recovered by effectively interpolating missing data at virtual transducers.

The consistency of the proposed imaging algorithm is examined by using the simple Born approximation for both forward and inverse models. Full numerical simulations are then run on a series of wave-speed maps converted from realistic corrosion patches, and the HARBUT algorithm is effectively incorporated into the iteration of virtual transducers, showing significant improvements in resolution and in the estimate of extreme values as well. An experiment is performed with the guided wave tomography technique, to further validate the developed imaging scheme. In the future, more complex specimens will be considered for further evaluation of the developed methodology.

The proposed methodology for DT of wave-speed map with undersampled data provides significant potential for applications in ultrasonic imaging, especially for guided wave tomography to reconstruct the corrosion profiles. Having sufficient numbers of sensors for conventional array imaging, satisfying the sampling criterion is always expensive. Furthermore, in a real measurement setup, deploying a large number of transducers is often practically challenging due to geometrical limitations. The proposed imaging method requires significantly fewer sensors (e.g., at least 50% reduction in this paper), and therefore, can be applied for design of low-cost ultrasonic arrays and also more convenient measurement setup.

References

[1] Z. Fan, A. F. Mark, M. J. S. Lowe, and P. J. Withers, "Nonintrusive estimation of anisotropic stiffness maps of heterogeneous steel welds for the improvement of ultrasonic array inspection," *IEEE Trans. Ultrason., Ferroelect., Freq. Control*, vol. 62, no. 8, pp. 1530–1543, Aug. 2015.

[2] P. Huthwaite and F. Simonetti, "High-resolution imaging without iteration: A fast and robust method for breast ultrasound tomography," *J. Acoust. Soc. Amer.*, vol. 130, no. 3, pp. 1721–1734, 2011.

[3] Z. Chen, A. Basarab, and D. Kouamé, "Compressive deconvolution in medical ultrasound imaging," *IEEE Trans. Med. Imag.*, vol. 35, no. 3, pp. 728–737, Mar. 2016.

[4] J. S. Schreiman, J. J. Gisvold, J. F. Greenleaf, and R. C. Bahn, "Ultrasound transmission computed tomography of the breast," *Radiology*, vol. 150, no. 2, pp. 523–530, 1984.

[5] P. Belanger and P. Cawley, "Feasibility of low frequency straight-ray guided wave tomography," *NDT E Int.*, vol. 42, pp. 113–119, Mar. 2009.

[6] N. Ozmen, R. Dapp, M. Zapf, H. Gemmeke, N. V. Ruiter, and K. W. van Dongen, "Comparing different ultrasound imaging methods for breast cancer detection," *IEEE Trans. Ultrason., Ferroelect., Freq. Control*, vol. 62, no. 4, pp. 637–646, Apr. 2015.

[7] L. Huang, F. Simonetti, and N. Duric, "A multiscale approach to diffraction tomography of complex three-dimensional objects," *Appl. Phys. Lett.*, vol. 95, no. 6, p. 061904, 2007.

[8] X. Pan and M. A. Anastasio, "On a limited-view reconstruction problem in diffraction tomography," *IEEE Trans. Med. Imag.*, vol. 21, no. 4, pp. 413–416, Apr. 2002.

[9] P. Huthwaite and F. Simonetti, "High-resolution guided wave tomography," *Wave Motion*, vol. 50, no. 5, pp. 979–993, 2013.

[10] A. J. Brath, F. Simonetti, P. B. Nagy, and G. Instanes, "Experimental validation of a fast forward model for guided wave tomography of pipe elbows," *IEEE Trans. Ultrason., Ferroelect., Freq. Control*, vol. 64, no. 5, pp. 859–871, May 2017.

[11] R. Wu and M. N. Toksöz, "Diffraction tomography and multisource holography applied to seismic imaging," *Geophysics*, vol. 52, no. 1, pp. 11–25, 1987.

[12] W. Munk and C. Wunsch, "Ocean acoustic tomography: A scheme for large scale monitoring," *Deep Sea Res. A, Oceanograph. Res. Papers*, vol. 26, no. 2, pp. 123–161, 1979.

[13] N. Quaegebeur, P. Masson, D. Langlois-Demers, and P. Micheau, "Dispersion-based imaging for structural health monitoring using sparse and compact arrays," *Smart Mater. Struct.*, vol. 20, no. 2, pp. 1–12, 2011.

[14] A. Velichko, "Optimization of guided wave array for inspection of large plate structures," in *Proc. AIP Conf.*, vol. 35, 2016, p. 030005.

[15] Y. Sung, W. Choi, C. Fang-Yen, K. Badizadegan, R. R. Dasari, and M. S. Feld, "Optical diffraction tomography for high resolution live cell imaging," *Opt. Exp.*, vol. 17, no. 1, pp. 266–277, 2009.

[16] F. J. Herrmann, M. P. Friedlander, and O. Yilmaz, "Fighting the curse of dimensionality: Compressive sensing in exploration seismology," *IEEE Signal Process. Mag.*, vol. 29, no. 3, pp. 88–100, May 2012.

[17] S. N. Ramadas, J. Jackson, J. Dziewierz, R. O'Leary, and A. Gachagan, "Application of conformal map theory for design of 2-D ultrasonic array structure for NDT imaging application: A feasibility study," *IEEE Trans. Ultrason., Ferroelect., Freq. Control*, vol. 61, no. 3, pp. 496–504, Mar. 2014.

[18] N. Quaegebeur and P. Masson, "Correlation-based imaging technique using ultrasonic transmit-receive array for non-destructive evaluation," *Ulrasonics*, vol. 52, no. 8, pp. 1056–1064, 2012.

[19] D. Verhoeven, "Limited-data computed tomography algorithms for the physical sciences," *Appl. Opt.*, vol. 32, no. 20, pp. 3736–3754, 1993.

[20] J. Romberg, "Imaging via compressive sampling," *IEEE Signal Process. Mag.*, vol. 25, no. 2, pp. 14–20, Mar. 2008.

[21] E. J. Candes, J. Romberg, and T. Tao, "Robust uncertainty principles: Exact signal reconstruction from highly incomplete frequency information," *IEEE Trans. Inf. Theory*, vol. 52, no. 2, pp. 489–509, Feb. 2006.

[22] E. J. Candès and M. B. Wakin, "An introduction to compressive sampling," *IEEE Signal Process. Mag.*, vol. 25, no. 2, pp. 21–30, Mar. 2008.

[23] E. Y. Sidky, C.-M. Kao, and X. Pan, "Accurate image reconstruction from few-views and limited-angle data in divergent-beam CT," *J. X-RAY Sci. Technol.*, vol. 14, no. 2, pp. 119–139, 2006.

[24] E. Y. Sidky and X. Pan, "Image reconstruction in circular cone-beam computed tomography by constrained, total-variation minimization," *Phys. Med. Biol.*, vol. 53, no. 17, p. 4777, 2008.

[25] M. Lustig, D. Donoho, and J. M. Pauly, "Sparse MRI: The application of compressed sensing for rapid MR imaging," *Magn. Reson. Med.*, vol. 58, no. 6, pp. 1182–1192, 2007.
[26] S. Ravishankar and Y. Bresler, "MR image reconstruction from highly undersampled k-space data by dictionary learning," *IEEE Trans. Med. Imag.*, vol. 30, no. 5, pp. 1028–1041, May 2011.
[27] A. G. J. Besson *et al.*, "A sparse reconstruction framework for Fourier-based plane-wave imaging," *IEEE Trans. Ultrason., Ferroelect., Freq. Control*, vol. 63, no. 12, pp. 2092–2106, Dec. 2016.
[28] N. Wagner, Y. C. Eldar, and Z. Friedman, "Compressed beamforming in ultrasound imaging," *IEEE Trans. Signal Process.*, vol. 60, no. 9, pp. 4643–4657, Sep. 2012.
[29] J. Provost and F. Lesage, "The application of compressed sensing for photo-acoustic tomography," *IEEE Trans. Med. Imag.*, vol. 28, no. 4, pp. 585–594, Apr. 2009.
[30] K. C. Tam and V. Perez-Mendez, "Tomographical imaging with limited-angle input," *J. Opt. Soc. Amer.*, vol. 71, no. 5, pp. 582–592, 1981.
[31] P. Huthwaite, A. A. Zwiebel, and F. Simonetti, "A new regularization technique for limited-view sound-speed imaging," *IEEE Trans. Ultrason., Ferroelect., Freq. Control*, vol. 60, no. 3, pp. 603–613, Mar. 2013.
[32] P. Huthwaite, "Guided wave tomography with an improved scattering model," *Proc. Roy. Soc. A, Math., Phys. Eng. Sci.*, vol. 472, no. 2195, pp. 1–24, 2016.
[33] A. C. Kak and M. Slaney, *Principles of Computerized Tomographic Imaging*. New York, NY, USA: IEEE Press, 1988. [Online]. Available: http://www.slaney.org/pct/pct-toc.html
[34] P. Huthwaite, "Quantitative imaging with mechanical waves," Ph.D. dissertation, Dept. Mech. Eng. Imperial College London, Kensington, London, 2012. [Online]. Available: https://spiral.imperial.ac.uk/handle/10044/1/9765
[35] P. Huthwaite, "Improving accuracy through density correction in guided wave tomography," *Proc. Math. Phys. Eng. Sci.*, vol. 472, no. 2186, p. 20150832, 2016.
[36] F. Simonetti and L. Huang, "From beamforming to diffraction tomography," *J. Appl. Phys.*, vol. 103, no. 10, p. 103110, 2008.
[37] P. Huthwaite, "Eliminating incident subtraction in diffraction tomography," *Proc. Roy. Soc. A, Math., Phys. Eng. Sci.*, vol. 472, no. 2195, p. 20160707, 2016.
[38] R. Lavarello and M. Oelze, "A study on the reconstruction of moderate contrast targets using the distorted born iterative method," *IEEE Trans. Ultrason., Ferroelect., Freq. Control*, vol. 55, no. 1, pp. 112–124, Jan. 2007.
[39] S. Li, K. Mueller, M. Jackowski, D. P. Dione, and L. H. Staib, "Fast marching method to correct for refraction in ultrasound computed tomography," in *Proc. 3rd IEEE Int. Symp. Biomed. Imag., Nano Macro*, Apr. 2006, pp. 896–899.
[40] F. Simonetti, L. Huang, and N. Duric, "On the spatial sampling of wave fields with circular ring apertures," *J. Appl. Phys.*, vol. 101, no. 8, p. 083103, 2007.
[41] A. Papoulis, "A new algorithm in spectral analysis and band-limited extrapolation," *IEEE Trans. Circuits Syst.*, vol. CAS-22, no. 9, pp. 735–742, Sep. 1975.
[42] A. V. Oppenheim and R. W. Schafer, *Discrete-Time Signal Processing*, 2nd ed. Englewood Cliffs, NJ, USA: Prentice-Hall, 1999.
[43] P. Huthwaite, "Evaluation of inversion approaches for guided wave thickness mapping," *Proc. Roy. Soc. A, Math., Phys. Eng. Sci.*, vol. 470, no. 2166, pp. 1–28, 2014.
[44] J. A. Roden and S. D. Gedney, "Convolution PML (CPML): An efficient FDTD implementation of the CFS–PML for arbitrary media," *Microw. Opt. Technol. Lett.*, vol. 27, no. 5, pp. 334–339, 2000.
[45] J. R. Pettit, A. Walker, P. Cawley, and M. J. S. Lowe, "A stiffness reduction method for efficient absorption of waves at boundaries for use in commercial finite element codes," *Ultrasonics*, vol. 54, no. 7, pp. 1868–1879, 2014.
[46] P. Huthwaite, "Accelerated finite element elastodynamic simulations using the GPU," *J. Comput. Phys.*, vol. 257, pp. 687–707, Jan. 2014.
[47] P. Belanger, P. Cawley, and F. Simonetti, "Guided wave diffraction tomography within the born approximation," *IEEE Trans. Ultrason., Ferroelect., Freq. Control*, vol. 57, no. 6, pp. 1405–1418, Jun. 2010.

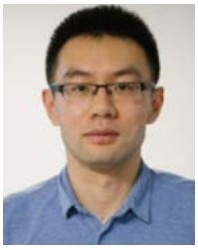

Fan Shi received the B.Sc. degree in acoustics from Nanjing University, the M.Sc. degree in electrical and computer engineering from the Georgia Institute of Technology, Atlanta, GA, USA, and the Ph.D. degree in mechanical engineering from Imperial College London, London, U.K.

He is currently a Post-Doctoral Research Associate with the Department of Mechanical Engineering, Imperial College. His current research interest include elastic wave scattering theory, scattering from rough surfaces, defect detection/characterization, numerical modelling of waves, and ultrasonic imaging for nondestructive evaluation.

Peter Huthwaite received the M.Eng. and Ph.D. degrees in mechanical engineering from Imperial College London, London, U.K.

In 2016, he was a Lecturer of mechanical engineering with Imperial College London, where he leads imaging research and has undertaken extensive research on improving imaging algorithms, particularly for guided wave tomography with the Non-Destructive Testing Group. His main research interests include limited data imaging for ultrasonics and radiography, to reduce issues associated with acquisition time, system complexity, and physical restrictions that occur in practice. His current research interests include the development of quantitative image reconstruction algorithms, with applications in medicine for breast cancer diagnosis and nondestructive testing for early stage damage detection, as well as the numerical modeling of waves, and GPU-based finite-element software package Pogo.